

# Mix3R: Mixing Feed-forward Reconstruction and Generative 3D Priors for Joint Multi-view Aligned 3D Reconstruction and Pose Estimation

Siyu Lin  
Tsinghua University  
Beijing, China  
linsy21@mails.tsinghua.edu.cn

Zhou Xue  
Tsinghua University  
Beijing, China  
xuezhou08@gmail.com

Hongwen Zhang  
Beijing Normal University  
Beijing, China  
zhanghongwen@bnu.edu.cn

Liang An  
Tsinghua University  
Beijing, China  
anliang@mail.tsinghua.edu.cn

Dongping Li  
ByteDance  
Hangzhou, China  
lidongping83@gmail.com

Shaohui Jiao  
ByteDance  
Beijing, China  
jiaoshaohui@bytedance.com

Yebin Liu  
Tsinghua University  
Beijing, China  
liuyebin@mail.tsinghua.edu.cn

## Abstract

Recent trends in sparse-view 3D reconstruction have taken two different paths: feed-forward reconstruction (such as VGGT) that predicts pixel-aligned point maps without a complete geometry, and generative 3D reconstruction (such as TRELLIS) that generates complete geometry but often with poor input-alignment. We present Mix3R, a novel generative 3D reconstruction method which mixes feed-forward reconstruction and 3D generation into a single framework in an aligned manner. Mix3R generates a 3D shape in two stages: a sparse voxel generation stage and a textured geometry generation stage. Unlike pure generative methods, our first-stage generation jointly produces a coarse 3D structure (sparse voxels), per-view point maps and camera parameters aligned to that 3D structure. This is made possible by introducing a Mixture-of-Transformers architecture that inserts global self-attentions to a feed-forward reconstruction model and a 3D generative model, both pretrained on large-scale data. This design effectively retains the pretrained priors but enables better 2D-3D alignment. Based on the initial aligned generations of sparse 3D voxels and point maps, we compute an overlap-based attention bias that is directly added to another pretrained textured geometry generation model, enabling it to correctly place input textures onto generated shapes in a training-free manner. Our design brings mutual benefits to both feed-forward reconstruction and 3D generation: The feed-forward branch

learns to ground its predictions to a generative 3D prior, and conversely, the 3D generation branch is conditioned on geometrically informative features from the feed-forward branch. As a result, our method produces 3D shapes with better input alignment compared with pure 3D generative methods, together with camera pose estimations more accurate than previous feed-forward reconstruction methods. Our project page is at <https://jsnl.n.githhub.io/mix3r/>

## 1. Introduction

3D reconstruction and camera pose estimation from multi-view images is an important technique for 3D asset acquisition and spatial perception. Traditional multi-view 3D reconstruction methods such as COLMAP [44, 45] require a dense camera set and feature matching techniques to recover the point cloud geometry and camera parameters. Despite their accuracy, these methods usually have high computational complexity and cannot adapt to extreme cases such as sparse views. Recently, two new types of 3D reconstruction have gradually taken over the research trend: feed-forward reconstruction and generative reconstruction.

A common approach taken by feed-forward reconstruction methods (e.g., VGGT [55],  $\pi^3$  [61], MapAnything [23] and DepthAnything3 [32]) is to directly regress pixel-aligned attributes including depth maps, point maps or ray maps. Camera poses can also be predicted using dedicated

decoder heads or inferred from point maps [27]. The pixel-aligned design of feed-forward methods generally produces good input-alignment, but also brings the natural drawback that they only reconstruct the seen part and strongly relies on overlaps between input views. For sparse views, they would produce inaccurate or incomplete reconstructions. On the other hand, 3D generative models [6, 29, 30, 51–53, 62, 64, 65, 67, 68, 75] allow modeling multi-view reconstruction as an image-conditioned generation process. Despite the visually pleasant generated shapes, they are merely look-alikes of the input and may not faithfully preserve the geometric dimensions and texture details because they lack explicitly aligned control signals during the injection of image conditions.

A few recent advances attempt to incorporate reconstruction, generation and pose estimation into one single task. ReconViaGen [3] injects VGGT [55] features into the generation process to improve input alignment. CUPID [17] jointly generates a UV voxel volume from which camera poses can be solved using PnP. While it demonstrated the ability of a multi-view extension using multi-diffusion [1], theoretically this lacks inter-view knowledge to handle rotationally symmetric shapes with asymmetric textures.

Despite these efforts, we would like to ask: How can we unify feed-forward reconstruction and generative reconstruction in a mutually beneficial way? The key difficulty lies in their *mutual alignment*. If a feed-forward model already has the knowledge of the underlying 3D shape, then it can ground its predictions to that shape instead of relying on image overlaps. Conversely, if a generative reconstruction model is conditioned on known camera poses, we can leverage fine-grained pixel alignment to generate 3D shapes that better match the input images. This is a chicken-and-egg problem.

To tackle these issues, we propose *Mix3R*, a novel method that achieves aligned feed-forward reconstruction and generative reconstruction in a mutually beneficial way. Our framework adopts a two-stage coarse-to-fine pipeline following TRELIS [68]. Given multi-view input images of an object, the first stage jointly generates a coarse 3D shape and predicts point maps and camera poses in an aligned manner, and the second stage generates more detailed geometry with input-aligned texture utilizing the alignment from the first stage. In the first stage, we design a mixture-of-transformers (MoT) [31] architecture for TRELIS [68] and  $\pi^3$  [61] and train it to predict aligned voxels and point maps. In the second stage, we design an attention bias based on the overlaps between 3D voxels and 2D image patches. In a training-free manner, the attention bias is added on top of a pretrained flow model to generate the final 3D asset but with more accurately aligned control.

Our designs lead to mutual benefits for both feed-forward reconstruction and 3D generation. The information

exchange in the MoT architecture allows the feed-forward branch to learn to ground its predictions to a generative 3D prior, and conversely, the 3D generation branch is now conditioned on geometrically informative features from the feed-forward branch. As a result, our method produces 3D assets with better input alignment compared with pure 3D generative methods, together with camera pose estimations more accurate than previous feed-forward reconstruction methods. In summary, our contributions are as follows.

- We propose *Mix3R*, a novel framework that effectively unifies 3D generation and feed-forward reconstruction in an aligned manner, by fusing two pretrained models from each domain to achieve joint geometry generation and camera pose estimation. Unlike ReconViaGen which is a one-way process of injecting VGGT features into generation, our architecture is designed so that they become mutually beneficial.
- To best utilize existing pretrained models, we design a mixture-of-transformers (MoT) architecture to incorporate the priors of a feed-forward reconstruction model ( $\pi^3$ ) and a 3D generative model (TRELIS). Our MoT design mutually benefits both branches in terms of alignment by allowing information exchange between the generative 3D prior and geometrically informative pixel-aligned features.
- To further improve alignment in the final textured geometry generation, we propose an attention bias based on the overlaps between the generated coarse voxels and the aligned image patches. The attention bias is added to a pretrained textured geometry flow model in a training-free manner, boosting the quality with minimal extra cost.

## 2. Related Work

We categorize 3D reconstruction methods into two categories: generative reconstruction which utilizes conditional generative models to produce actual 3D models from images, and feed-forward reconstruction which directly maps one or more input images to 3D.

### 2.1. Generative Reconstruction

There has been a number of 3D generation methods based on different generative frameworks, e.g., GANs [2, 10, 12, 48, 63, 82] and diffusion models [4, 14, 16, 34, 36, 46, 47, 50, 59, 77, 78]. While some works are purely generative, others allow conditioned generation and can thus be used as a generative reconstruction method. Early methods mainly focus on simple representations such as point clouds [34, 46], tri-planes [2, 47, 59, 77] and volumes [16, 36, 50], and the quality of their generated models are limited by factors such as point number and volume resolution. As a result, these methods cannot produce asset-level 3D objects.

Recently, inspired by latent diffusion models on images [40], 3D generation also started using latent-space gen-

eration. A natural and common choice of latent representation is sparse voxels [6, 30, 62, 64, 65, 68, 75], which, upon generation, can be further decoded to different 3D representations such as meshes, 3D Gaussians [24] or radiance fields [35]. Another popular choice of compression is VecSet [76], which encodes 3D shapes into vectors for better compression. Building on the VecSet representation, a number of works are capable of generating high-quality 3D assets [29, 51–53, 80].

Among these works, closest to ours is image-conditioned generative models, e.g., TRELLIS [68]. However, methods like TRELLIS only injects images conditions using cross attention modules without explicit view-object alignment. As a result, the generated models may not align well with the input image signal.

## 2.2. Feed-forward Reconstruction

Unlike generative reconstruction which directly models the data distribution (usually embedded with a normalized coordinate system), feed-forward reconstructions directly regresses the target geometry. These methods are mostly *pixel-aligned*. For example, Saito et al. [41, 42], Xiu et al. [69, 70] use pixel-aligned image features for monocular human reconstruction, achieving good input alignment but often fail for unseen regions. To alleviate this, reconstructions must consider multi-view inputs, which requires either direct or indirect pose estimation. Early work such as FORGE [19] estimates poses to fuse multi-view features into a unified feature space and then decodes it into a NeRF [35] volume. Recently, point map regression became the trending paradigm of feed-forward methods. Pioneer work DUST3R [58] directly regresses stereo point maps in a Siamese manner. MonST3R [79] extends it to dynamic scenes using the same paradigm. Subsequent methods CUT3R [57] and TTT3R [5] employs a latent state to further support long-term streaming. Unlike these methods which rely on image pairs or image-latent pairs, VGGT [55] and its follow-up works [23, 61] directly regress point maps and camera poses from an entire image collection. Follow-up works extend this pixel-aligned point map prediction paradigm to predicting 3D Gaussians for rendering purposes [21, 60, 73]. Despite being able to estimate camera poses from sparse views, these methods only reconstruct seen regions and requires enough image overlap and coverage for good reconstruction quality.

Other than pixel-aligned feed-forward methods, there also exist feed-forward method that do not consider explicit multi-view alignment. For example, LRM [15], LEAP [20] and PF-LRM [56] predict a NeRF [35] volume from monocular or multi-view images. InstantMesh [72] uses multi-view image diffusion and LRM in a cascaded manner for better multi-view support. SpaRP [71] utilizes Stable Diffusion [40] to generate multi-view point maps and RGB im-

ages at given poses with unconstrained input views, turning pose-free reconstruction into traditional MVS with known cameras. Due to the lack of explicit input-output alignment and stochastic modeling of unseen regions, these methods often produces less aligned geometries or blurry textures.

## 2.3. Unifying Reconstruction and Generation

Attempts have been made to unify feed-forward reconstruction and generation. CAST [74] and SAM3D [43] can be conditioned on depth maps to generate shapes and estimate poses that closely match the input images. However, both CAST and SAM3D focus on single-view multi-object composition, not multi-view alignment and fusion. Recently, ReconViaGen [3] incorporates multi-view reconstruction guidance from the feed-forward model VGGT [55] to further enhance alignment. Concurrently, CUPID [17] jointly generates a UV voxel grid to solve for view-object alignment and use it for better texture generation. Focusing on scenes, Gen3R [18] and Aether [83] also explored unifying video generation and dynamic reconstruction in the sense that the former can be repurposed to achieve the latter. However, these are less related to our object-centric setting.

## 3. Method

### 3.1. Preliminaries: TRELLIS and $\pi^3$

Our goal is to achieve 3D generation and camera pose estimation from multi-view images in a unified and aligned manner. We build our model upon two existing models with large-scale pretraining: TRELLIS [68] and  $\pi^3$  [61]. We begin with a short introduction to them.

TRELLIS is a 3D generative model based on flow matching [33]. TRELLIS models each 3D shape using a structured latent representation: a set of features  $\{\mathbf{f}_i\}_{i=1}^L$  attached to the non-zero voxels  $\{\mathbf{p}_i\}_{i=1}^L$  of an occupancy grid  $\mathbf{O} \in \{0, 1\}^{64^3}$ . For simplicity, we use  $\mathbf{f} = \{(\mathbf{f}_i, \mathbf{p}_i)\}$  to represent a structured latent. Each  $\mathbf{f}$  can be further decoded into a mesh surface, a 3DGS [24] point cloud or a NeRF [35] using dedicated decoders. TRELLIS generates a 3D asset in two stages. First, a sparse structure latent code  $\mathbf{z} \in \mathbb{R}^{16^3 \times 8}$  is generated using a flow transformer  $\mathcal{F}_{ss}$ . Then, a sparse structure decoder  $\mathcal{D}_{ss}$  decodes  $\mathbf{z}$  into an occupancy grid  $\mathbf{O} = \mathcal{D}_{ss}(\mathbf{z})$ . Non-empty voxels  $\{\mathbf{p}_i\}_{i=1}^L$  are then extracted from  $\mathbf{O}$ . A second sparse flow transformer  $\mathcal{F}_{slat}$  then generates a structured latent code  $\mathbf{f}$  on  $\{\mathbf{p}_i\}_{i=1}^L$ . Both  $\mathcal{F}_{ss}$  and  $\mathcal{F}_{slat}$  use cross-attention to inject image conditions and employ standard Euler sampler during generation.

$\pi^3$  [61] is a feed-forward reconstruction method. Given images  $\{\mathbf{I}_i\}_{i=1}^N$ ,  $\pi^3$  processes them using a permutation invariant vision transformer and obtain camera-space point maps  $\mathbf{X}_i \in \mathbb{R}^{H \times W \times 3}$  camera poses in the form of camera-to-world transformations  $(\mathbf{R}_i, \mathbf{T}_i) \in \text{SE}(3)$ . World-space point maps can be obtained as  $\mathbf{R}_i(\mathbf{X}_i) + \mathbf{T}_i$ , where  $(\mathbf{R}_i, \mathbf{T}_i)$

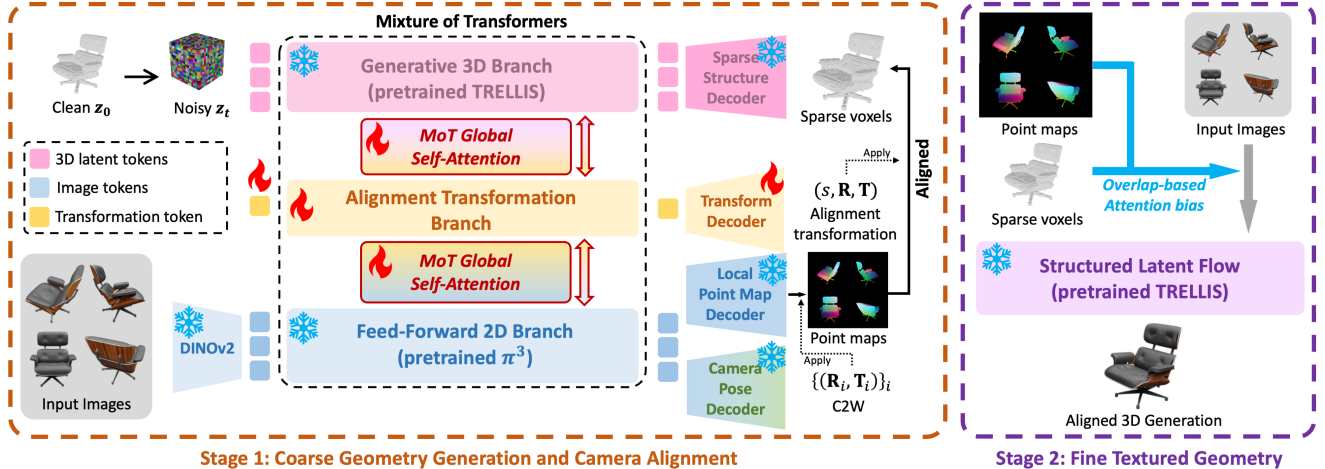


Figure 1. The overall architecture of our two-stage framework. Given multi-view unposed input images, we first employ a mixture-of-transformers architecture that jointly infers a coarse 3D structure, pixel-aligned local point maps, camera poses, and an alignment transformation that aligns point maps to the 3D shape. This alignment is then used to provide fine-grained control in the form of attention bias for the final 3D asset generation.

applies to each pixel in  $\mathbf{X}_i$  independently. Since  $\pi^3$  has an input permutation invariant design, and  $\mathbf{X}_i, \mathbf{R}_i, \mathbf{T}_i$  are trained with affine-invariant losses, the output distribution of  $\pi^3$  is generally more stable compared with reference frame-based methods such as VGGT [55].

### 3.2. Joint Coarse Geometry Generation and Camera Pose Estimation

The overall architecture is shown in Fig. 1. Our stage-1 model jointly generates a coarse 3D structure and camera poses aligned to it. To best utilize existing pretrained models, we choose the TRELIS sparse structure flow model as our generative branch (3D branch) and the  $\pi^3$  backbone transformer as our feed-forward branch (2D branch). Note that TRELIS and  $\pi^3$  have different output coordinate spaces. Thus, we add an extra transformation branch and a decoder head to predict a similarity transform  $(s, \mathbf{R}, \mathbf{T})$  that aligns the output of  $\pi^3$  to the voxel space of TRELIS. These branches are incorporated into a single large transformer using the MoT paradigm [31]. We will explain the inputs and outputs of the model in this section. Specific architectural designs are deferred to Sec 3.3.

Let  $\mathcal{F}_{\text{mix}}$  denote our stage-1 network. For notational simplicity, we assume the DINOv2 encoder [8, 22, 37], the main transformer blocks and all the decoders shown in Fig. 1 are represented by  $\mathcal{F}_{\text{mix}}$ . The network  $\mathcal{F}_{\text{mix}}$  takes the following inputs: (1) a noisy sparse structure latent code

$$\mathbf{z}_t = (1 - t)\mathbf{z}_0 + t\epsilon, t \in [0, 1] \quad (1)$$

where  $\mathbf{z}_0$  is its corresponding clean latent code,  $\epsilon$  is a Gaussian noise vector having the same dimensions, and  $t$  is the time step used in standard flow matching [33]; (2)

multi-view images  $\{\mathbf{I}_i\}_{i=1}^N$  of the 3D shape corresponding to  $\mathbf{z}_0$ ; (3) A learnable token  $\mathbf{g}$  representing the alignment transformation  $(s, \mathbf{R}, \mathbf{T})$ . Following the flow matching paradigm [33], the 3D branch predicts a velocity  $\mathbf{v}$ , which is trained to match  $\epsilon - \mathbf{z}_0$ . The image tokens of  $\{\mathbf{I}_i\}_{i=1}^N$  are processed by the 2D branch and then decoded into local point maps  $\{\mathbf{X}_i\}_{i=1}^N$  and camera poses  $\{(\mathbf{R}_i, \mathbf{T}_i)\}_{i=1}^N$ . We can write down the whole network as:

$$\mathbf{v}, \{\mathbf{X}_i\}, \{(\mathbf{R}_i, \mathbf{T}_i)\}, (s, \mathbf{R}, \mathbf{T}) = \mathcal{F}_{\text{mix}}(\mathbf{z}_t, t, \{\mathbf{I}_i\}, \mathbf{g}). \quad (2)$$

For training,  $\mathbf{v}$  is supervised by the standard flow matching loss

$$\mathcal{L}_{\text{fm}} = \|\mathbf{v} - (\epsilon - \mathbf{z}_0)\|^2. \quad (3)$$

For the output point maps, camera poses and the alignment transformation, instead of supervising them separately, we first compute the point maps after applying these transformations:

$$\hat{\mathbf{X}}_i = s(\mathbf{R}(\mathbf{R}_i(\mathbf{X}_i) + \mathbf{T}_i) + \mathbf{T}). \quad (4)$$

All the aligned point maps  $\{\hat{\mathbf{X}}_i\}$  are supervised by two losses  $\mathcal{L}_{\text{pts}}$  and  $\mathcal{L}_{\text{nmf}}$  between them and the ground truth point maps. Here,  $\mathcal{L}_{\text{pts}}$  is the L1 loss on point coordinates, and  $\mathcal{L}_{\text{nmf}}$  is the L1 loss on point normals computed from point maps. The final loss is

$$\mathcal{L} = \mathcal{L}_{\text{fm}} + \lambda_{\text{pts}}\mathcal{L}_{\text{pts}} + \lambda_{\text{nmf}}\mathcal{L}_{\text{nmf}}. \quad (5)$$

Note that our goal is to align point maps  $\{\hat{\mathbf{X}}_i\}$  to the shape  $\mathbf{z}_0$ . However, since the network  $\mathcal{F}_{\text{mix}}$  only sees the noisy version  $\mathbf{z}_t$ . When  $t$  is large, almost no geometric information is retained in  $\mathbf{z}_t$  and the losses  $\mathcal{L}_{\text{pts}}$ ,  $\mathcal{L}_{\text{nmf}}$  become

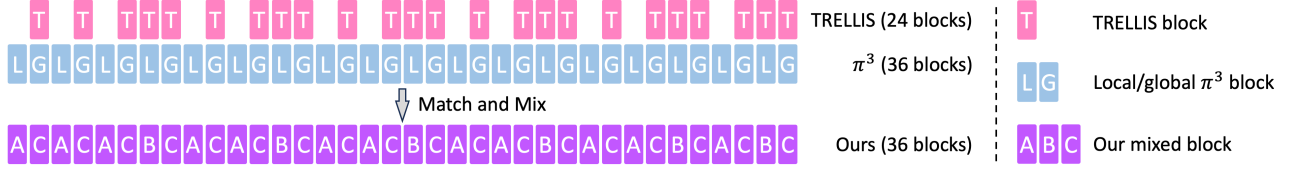


Figure 2. The block matching configuration of our MoT architecture. According to different matching types, our network has three different types of mixed blocks.

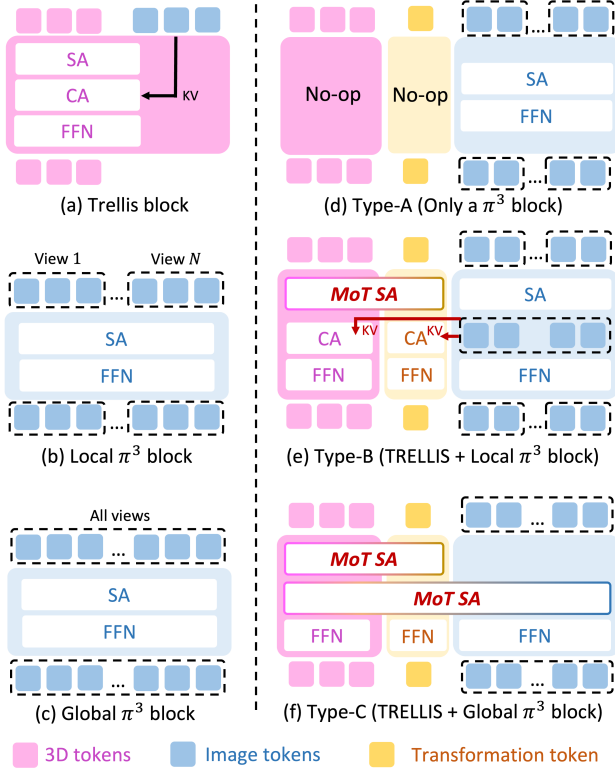


Figure 3. Illustrations of different block mixture architectures. Sub-figures (a), (b) and (c) on the left show the structures of the original TRELLIS blocks and  $\pi^3$  blocks, whereas (e), (f) and (g) show the three types of mixed blocks obtained from our block matching strategy in Sec. 3.3. Note that we still use residual connections, layer normalization, time step modulation and QK-norm, but do not show them in this figure for simplicity.

ambiguous. Therefore, we choose their coefficients to depend on  $t$ , and empirically set them as

$$\lambda_{pts} = \text{Sigmoid}(-24t + 9), \lambda_{nml} = 0.1 \times \lambda_{pts}. \quad (6)$$

Note that this implies  $t \geq 0.5 \implies \lambda_{pts} \approx 0$  and  $t \leq 0.25 \implies \lambda_{pts} \approx 1$ . This choice is based on an empirical observation that when  $t \geq 0.5$  almost no geometry can be recovered from  $\mathbf{z}_0$  using the sparse structure decoder of TRELLIS, while when  $t \leq 0.25$  the decoded geometry is mostly complete except for minor details.

### 3.3. Architectural Designs of the Mixture-of-Transformers Network

In this section, we explain our specific architectural designs. Our MoT network is a mixture of two pretrained models: the sparse structure flow transformer in TRELLIS [68] and the backbone transformer of  $\pi^3$  [61]. Fig. 3(a,b,c) show the original block structures of TRELLIS and  $\pi^3$ , respectively. Note that  $\pi^3$  follows VGGT [55] to alternate between local self-attention (different views are batched) and global self-attention (all views concatenated into a single token sequence). Thus,  $\pi^3$  has two types of blocks, local and global, as shown in Fig. 3(b,c).

We intend to design a mixed architecture that allows information exchange between TRELLIS and  $\pi^3$  by inserting self-attentions between them. While there might be different ways to fuse these two networks, enumerating them is not practical. Instead, we adopt a mixing scheme which best preserves pretrained weights, based on the following principles. (1) To retain the pretrained abilities of TRELLIS and  $\pi^3$  as much as possible (trying not to discard pretrained weights), we insert MoT [31] self-attentions since it uses different query/key/value matrices for different modalities. (2) To keep the alternating local/global attention design of  $\pi^3$ , we only extend the self-attention in  $\pi^3$ 's global blocks to MoT self-attentions, while local blocks remain local. (3) For simplicity, blocks for the alignment transformation branch adopts a symmetric structure to TRELLIS blocks.

Since TRELLIS has 24 blocks while  $\pi^3$  has 36 blocks, we need to define a block matching before inserting MoT attentions between them. Based on principle (2) above, we first guarantee every global  $\pi^3$  block is matched with a TRELLIS block by computing a uniform injection from the 18 global  $\pi^3$  blocks into the 24 TRELLIS blocks. Then, 6 TRELLIS blocks remain unmatched, but there is only a unique way to match them with the remaining local  $\pi^3$  blocks in an order-preserving way (see the supplementary material for details). Finally, this matching scheme leads to the exact matching shown in Fig. 2, with 3 types of block mixtures. Fig. 3(d) shows type-A matching, where a local  $\pi^3$  block is not matched with any TRELLIS block, in which case no mixing actually happens. Fig. 3(e) shows type-B matching, where a local  $\pi^3$  block is matched with a

TRELLIS block. In this case, we extend the original TRELLIS block self-attention to an MoT self-attention across 3D tokens and the transformation token. We also inject the intermediate geometry-informative token features of  $\pi^3$  into the 3D branch and the transformation branch using cross-attention modules. Fig. 3(f) shows type-C matching, where a global  $\pi^3$  block is matched with a TRELLIS block. In this case we further extend the original cross-attention module to a large global MoT self-attention which processes all three modalities at once.

During training, we freeze all parameters that have a pre-trained value and are not affected by our newly added modules. Other parameters are activated (see supplementary material for details). In this way, we retain the abilities of the pretrained models as much as possible but also enable different modalities to interact with each other to achieve a good alignment between the feed-forward reconstruction branch and the generation branch.

### 3.4. Attention Bias for Training-Free Tuning of Textured Geometry Generation and Camera Refinement

Given multi-view images  $\{I_i\}_{i=1}^N$ , we can use our model to jointly generate a sparse structure latent  $\mathbf{z}$ , camera poses  $\{(\mathbf{R}_i, \mathbf{T}_i)\}_{i=1}^N$  and the alignment transformation  $(s, \mathbf{R}, \mathbf{T})$ . Our next step is to utilize the 2D-3D alignment to generate view-aligned fine geometry and texture.

For the latent code  $\mathbf{z}$ , we first use pretrained TRELLIS sparse structure decoder  $\mathcal{D}_{ss}$  to obtain the corresponding occupancy grid  $\mathbf{O} = \mathcal{D}_{ss}(\mathbf{z})$  and extract its non-zero voxels  $\{\mathbf{p}_i\}_{i=1}^L$ . Then, following TRELLIS, a second flow transformer  $\mathcal{F}_{slat}$  takes a noisy structured latent as input and gradually denoises it to generate the final clean latent as described in Sec. 3.1. The image conditions  $\{\mathbf{I}_i\}_{i=1}^N$  are first encoded using DINOv2 [8, 22, 37] and then injected into  $\mathcal{F}_{slat}$  using cross-attention modules. Let us denote by  $\mathbf{f}$  the intermediate token set corresponding to the structured latent to be denoised, and denote by  $\mathbf{y}$  the token set of the input DINOv2 tokens. Then a pretrained cross-attention can be written as follows:

$$\begin{aligned} & \text{CrossAttn}(Q(\mathbf{f}), K(\mathbf{y}), V(\mathbf{y})) \\ = & \text{Softmax}\left(\frac{Q(\mathbf{f})K(\mathbf{y})^T}{\sqrt{d}}\right)V(\mathbf{y}), \end{aligned} \quad (7)$$

where  $d$  is the feature dimension. We attempt to find a bias matrix  $\mathbf{B}(\mathbf{f}, \mathbf{y})$  such that the modified attention

$$\text{Softmax}\left(\frac{Q(\mathbf{f})K(\mathbf{y})^T}{\sqrt{d}} + \mathbf{B}(\mathbf{f}, \mathbf{y})\right)V(\mathbf{y}) \quad (8)$$

makes tokens in  $\mathbf{f}$  attend more to relevant tokens in  $\mathbf{y}$ .

Note that each token  $\mathbf{f}_j$  in  $\mathbf{f}$  corresponds to a voxel  $\mathbf{p}_j$  while each token  $\mathbf{y}_k$  in  $\mathbf{y}$  corresponds to an image patch

of one of  $\{I_i\}$ . Let  $\{\hat{\mathbf{X}}_i\}$  be the aligned point maps as described in Eq. (4), and let  $\hat{\mathbf{x}}_k$  be the point set corresponding to the patch  $\mathbf{y}_k$  in  $\{\hat{\mathbf{X}}_i\}$ . For each voxel  $\mathbf{p}_j$ , we define its average point count (APC) as

$$\begin{aligned} & \text{APC}(\mathbf{p}_j) \\ = & \begin{cases} \frac{\sum_k |\mathbf{p}_j \cap \hat{\mathbf{x}}_k|}{\#\{k: |\mathbf{p}_j \cap \hat{\mathbf{x}}_k| > 0\}}, & |\mathbf{p}_j \cap \hat{\mathbf{x}}_k| > 0 \text{ for some } k \\ 0, & \text{otherwise} \end{cases} \end{aligned} \quad (9)$$

where  $|\mathbf{p}_j \cap \hat{\mathbf{x}}_k|$  is the number of points in  $\hat{\mathbf{x}}_k$  that are contained in voxel  $\mathbf{p}_j$ . The final attention bias  $\mathbf{B}(\mathbf{f}_j, \mathbf{y}_k)$  added to the score between  $\mathbf{f}_j$  and  $\mathbf{y}_k$  is

$$\mathbf{B}(\mathbf{f}_j, \mathbf{y}_k) = \alpha \max\left(\frac{|\mathbf{p}_j \cap \hat{\mathbf{x}}_k| - \text{APC}(\mathbf{p}_j)}{\max_k (|\mathbf{p}_j \cap \hat{\mathbf{x}}_k|) - \text{APC}(\mathbf{p}_j)}, 0\right). \quad (10)$$

where  $\alpha > 0$  is a scaling hyperparameter. In our experiments we choose  $\alpha = 5$ .

The idea behind Eq. (10) is that the attention score for  $(\mathbf{f}_j, \mathbf{y}_k)$  should be increased if  $\mathbf{y}_k$  has an overlap with  $\mathbf{f}_j$  above average among all image tokens. We also empirically found that decreasing the attention scores leads to degraded performance, and thus clip the biases to have a minimum of 0. Finally, these modified attention scores are used to tune the behavior of  $\mathcal{F}_{slat}$  in a training-free manner to generate the final structured latent, which is then decoded into a mesh and a 3DGS representation.

Recall that our model in stage 1 only predicts camera poses, but not the intrinsics. To further refine the camera parameters, we use the predicted poses as initial values and estimate the intrinsics by solving the perspective projection equation in least squares. Then, the intrinsics and extrinsics are jointly refined using the DRTK differentiable renderer [38] by minimizing the RGB loss and the mask loss between the rendered 3D mesh and input images. More details are in the supplementary material.

## 4. Experiments

### 4.1. Implementation Details

Our model is trained on a subset of the TRELLIS-500k dataset [68], containing 404354 objects. Due to the extreme high cost of the original TRELLIS data processing pipeline, we use TRELLIS to generate our training dataset. For training, we adopt pretrained weights whenever possible and only activate the parameters without a pretrained weight and those related to our newly added MoT self-attentions and cross-attentions. We use a learning rate of  $10^{-4}$  with cosine scheduling and train for 400k steps with a batch size of 16. Please refer to the supplementary material for more details.

### 4.2. Evaluation

Our work aims at jointly generating 3D objects and their alignment to input images. We evaluate our method over

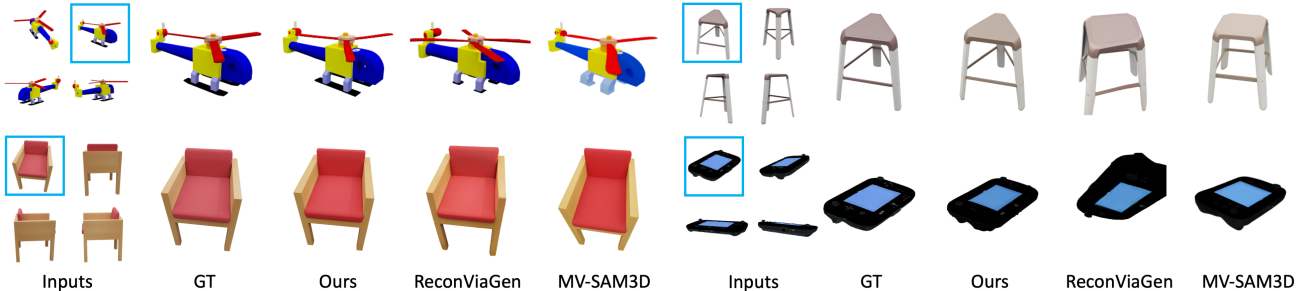


Figure 4. We exhibit the reprojection alignment. Each rendering result is obtained using the decoded 3D Gaussians and the predicted camera parameters.

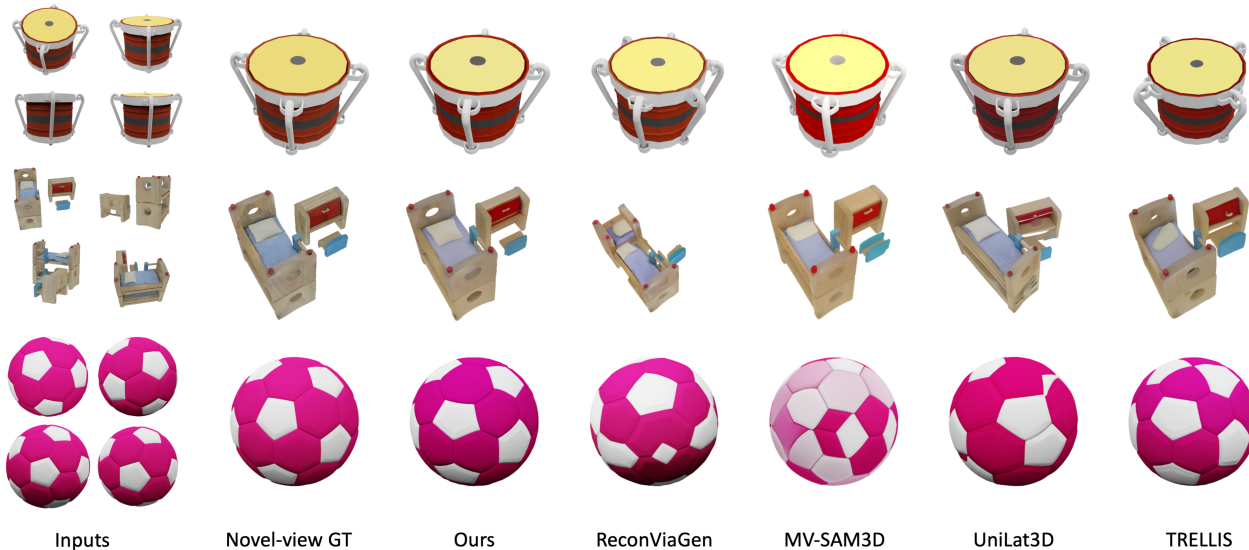


Figure 5. Qualitative results of novel-view rendering evaluation. We show input images and novel-view GT images. Our method more accurately restores texture and geometry.

Table 1. Metric evaluations for view-object alignment on the Toys4K and the GSO dataset.

| Dataset     | Toys4k        |               |              |
|-------------|---------------|---------------|--------------|
| Metric      | PSNR          | SSIM          | LPIPS        |
| MV-SAM3D    | 22.360        | 0.9168        | 0.065        |
| ReconViaGen | 23.834        | 0.9359        | 0.047        |
| Ours        | <b>28.144</b> | <b>0.9621</b> | <b>0.030</b> |
| Dataset     | GSO           |               |              |
| Metric      | PSNR          | SSIM          | LPIPS        |
| MV-SAM3D    | 22.345        | 0.9016        | 0.084        |
| ReconViaGen | 24.036        | 0.9260        | 0.058        |
| Ours        | <b>25.031</b> | <b>0.9281</b> | <b>0.057</b> |

three aspects: (1) input alignment; (2) geometry and texture accuracy; (3) camera pose accuracy; (4) real-world phone

captures. We use Toys4k [49] and Google Scanned Objects (GSO) [11] as evaluation datasets.

**Input alignment** In this experiment, we directly render the generated 3D models using predicted camera poses to measure how well the generated shape aligns with the input. This experiment simultaneously evaluates the quality of the generated shape and the accuracy of predicted camera poses, since both need to be accurate for the rendered images to be aligned with input images. We compare with ReconViaGen [3] and MV-SAM3D [28] since they both simultaneously generate geometry and pose, and both support multi-view inputs. Please refer to the supplementary material for baseline settings. Fig. 4 shows the qualitative results of the alignment evaluation. Our method not only generates geometry which is aligned with inputs but also estimates correct camera poses which allows accurate re-projection of the 3D shape back to input images, whereas

Table 2. Novel view synthesis and geometry evaluation.

| Dataset     | Toys4k        |               |              |                         | GSO           |               |              |                         |
|-------------|---------------|---------------|--------------|-------------------------|---------------|---------------|--------------|-------------------------|
| Metric      | PSNR          | SSIM          | LPIPS        | CD ( $\times 10^{-3}$ ) | PSNR          | SSIM          | LPIPS        | CD ( $\times 10^{-3}$ ) |
| TRELLIS     | 23.930        | 0.9311        | 0.055        | 7.9986                  | 22.420        | 0.9034        | 0.079        | 4.5658                  |
| UniLat3D    | 25.082        | 0.9415        | 0.049        | 7.0876                  | 22.765        | 0.9102        | 0.076        | 7.1384                  |
| MV-SAM3D    | 23.550        | 0.9273        | 0.059        | 2.7556                  | 22.331        | 0.9032        | 0.085        | 5.2356                  |
| ReconViaGen | 24.491        | 0.9335        | 0.046        | 1.9419                  | 24.183        | 0.9152        | 0.060        | 1.0015                  |
| Ours        | <b>27.177</b> | <b>0.9551</b> | <b>0.033</b> | <b>0.7419</b>           | <b>24.826</b> | <b>0.9271</b> | <b>0.055</b> | <b>0.7945</b>           |

the baseline methods ReconViaGen and MV-SAM3D can generate incorrect structures or wrong poses. We also report the metrics PSNR, SSIM and LPIPS [81] in Table 1. Our method performs the best in terms of input-alignment on both benchmark datasets.

**Geometry and texture accuracy** We also evaluate the quality of the generated 3D assets, regardless of the predicted camera poses. In this experiment, we additionally compare with TRELLIS [68], UniLat3D [62]. All metrics are computed after a similarity alignment to GT (see the supplementary material for details). For evaluating geometric accuracy, we measure the Chamfer distance (CD). For texture evaluation, we choose 4 novel views different from input views, and measure PSNR, SSIM and LPIPS for all novel-view renderings. Table 2 reports the quantitative results. Our generations score the best in terms of both geometry and texture accuracy. Fig. 5 shows some qualitative examples. Our lower Chamfer distance results indicate better preservation of object dimensions and their proportions, even though the visual appearances are sometimes similar to baseline methods. Our method also correctly places an asymmetric input texture onto symmetric shapes, whereas other methods are more likely to generate a plausible but misaligned texture. More results are presented in Fig. 6 and Fig. 7.

**Camera pose accuracy** We compare the accuracy of our camera pose estimation with ReconViaGen, MV-SAM3D, VGGT and  $\pi^3$ . Since camera poses can be ambiguous up to a similarity transformation, we evaluate the relative rotation accuracy (RRA), relative translation accuracy (RTA) and the area under curve (AUC) with an angle threshold of 30 degrees following Wang et al. [54]. Table 3 shows the evaluation results, where our method has the best overall performance compared with both feed-forward methods and generative methods.

**Real-world phone capture** Fig. 8 shows the generation results for real-world objects captured by cellphones. Our method performs comparably with ReconViaGen, while

Table 3. Quantitative evaluations of camera accuracy in terms of relative rotation accuracy (RRA), relative translation accuracy (RTA) and area under curve (AUC). All metrics use a threshold of 30 degrees.

| Dataset     | Toys4k       |              |              |
|-------------|--------------|--------------|--------------|
| Acc@30      | RRA          | RTA          | AUC          |
| VGGT        | 93.05        | 88.58        | 57.13        |
| $\pi^3$     | 91.71        | 88.72        | 57.72        |
| MV-SAM3D    | 65.73        | 67.22        | 31.88        |
| ReconViaGen | 82.63        | 85.04        | 49.83        |
| Ours        | <b>95.49</b> | <b>95.41</b> | <b>70.63</b> |
| Dataset     | GSO          |              |              |
| Acc@30      | RRA          | RTA          | AUC          |
| VGGT        | <b>97.78</b> | 91.36        | 60.20        |
| $\pi^3$     | 96.42        | 91.93        | 61.41        |
| MV-SAM3D    | 53.45        | 56.18        | 24.35        |
| ReconViaGen | 91.78        | 91.99        | 57.29        |
| Ours        | 93.50        | <b>94.50</b> | <b>66.93</b> |

other methods generally suffer from either geometry or texture distortions.

## 5. Summary

In this work, we propose Mix3R, a mixture of a pretrained 3D generative model and a 2D pixel-aligned feed-forward reconstruction model based on the MoT architecture [31]. Our model can jointly generate a sparse voxel structure and point maps aligned to it. Overlaps between the voxel structure and input images can be computed using the aligned point maps as an intermediary. Based on the availability of the overlap, we further compute an attention bias matrix such that the final geometry and texture generation attention correctly to different regions of input images. In this way, we successfully improve the input-alignment of generated 3D assets in terms of both geometry and texture accuracy.

Nonetheless, the model still faces limitations: (1) Even though the  $\pi^3$  branch provides geometrically informative features for the 3D branch, in cases where the test view



Figure 6. More qualitative results of novel-view rendering evaluation.

configuration deviates from the training distribution, it may actually disrupt the 3D branch and lead to degraded per-

formance. (2) Due to limited resources, our training utilizes TRELIS-generated training data, which do not con-

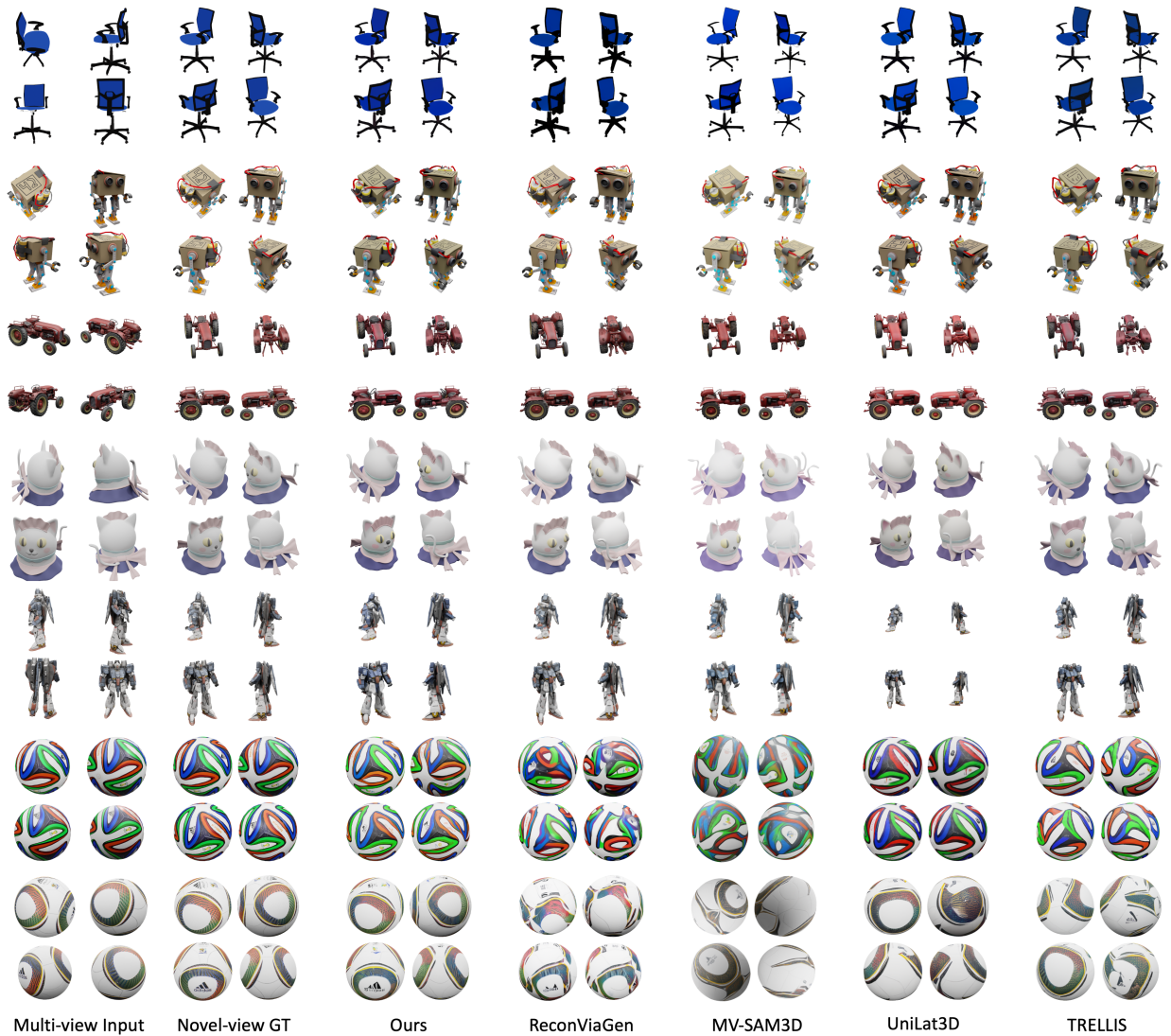


Figure 7. More qualitative results of novel-view rendering evaluation.

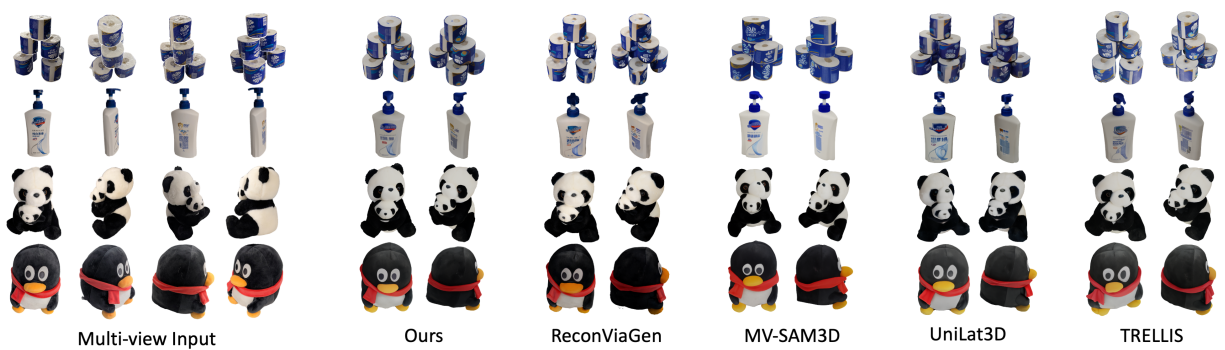


Figure 8. Qualitative results for real-world cellphone captures.

tain lighting or view-dependent visual effects. Directly applying our model to in-the-wild data can lead to degraded

performance. (3) The TRELIS VAE decoders are frozen in our paper, which means the generation quality is limited

by the pretrained TRELIS latent distribution. Please see the supplementary material for a more in-depth discussion and future directions.

## Acknowledgements

This work is supported by the National Science Foundation of China (NSFC) under Grant Number 62125107.

## References

- [1] Omer Bar-Tal, Lior Yariv, Yaron Lipman, and Tali Dekel. Multidiffusion: Fusing diffusion paths for controlled image generation. *arXiv preprint arXiv:2302.08113*, 2023. 2
- [2] Eric R. Chan, Connor Z. Lin, Matthew A. Chan, Koki Nagano, Boxiao Pan, Shalini De Mello, Orazio Gallo, Leonidas Guibas, Jonathan Tremblay, Sameh Khamis, Tero Karras, and Gordon Wetzstein. Efficient geometry-aware 3D generative adversarial networks. In *CVPR*, 2022. 2
- [3] Jiahao Chang, Chongjie Ye, Yushuang Wu, Yuantao Chen, Yidan Zhang, Zhongjin Luo, Chenghong Li, Yihao Zhi, and Xiaoguang Han. Reconviagen: Towards accurate multi-view 3d object reconstruction via generation. *arXiv preprint arXiv:2510.23306*, 2025. 2, 3, 7, 14, 15
- [4] Hansheng Chen, Jiatao Gu, Anpei Chen, Wei Tian, Zhuowen Tu, Lingjie Liu, and Hao Su. Single-stage diffusion nerf: A unified approach to 3d generation and reconstruction. In *ICCV*, 2023. 2
- [5] Xingyu Chen, Yue Chen, Yuliang Xiu, Andreas Geiger, and Anpei Chen. TTT3r: 3d reconstruction as test-time training. In *The Fourteenth International Conference on Learning Representations*, 2026. 3
- [6] Yiwen Chen, Zhihao Li, Yikai Wang, Hu Zhang, Qin Li, Chi Zhang, and Guosheng Lin. Ultra3d: Efficient and high-fidelity 3d generation with part attention, 2025. 2, 3
- [7] Jasmine Collins, Shubham Goel, Kenan Deng, Achleshwar Luthra, Leon Xu, Erhan Gundogdu, Xi Zhang, Tomas F. Yago Vicente, Thomas Dideriksen, Himanshu Arora, Matthieu Guillaumin, and Jitendra Malik. Abo: Dataset and benchmarks for real-world 3d object understanding. In *Proceedings of the IEEE/CVF Conference on Computer Vision and Pattern Recognition (CVPR)*, pages 21126–21136, 2022. 15
- [8] Timothée Darcet, Maxime Oquab, Julien Mairal, and Piotr Bojanowski. Vision transformers need registers, 2023. 4, 6
- [9] Matt Deitke, Ruoshi Liu, Matthew Wallingford, Huong Ngo, Oscar Michel, Aditya Kusupati, Alan Fan, Christian Laforte, Vikram Voleti, Samir Yitzhak Gadre, Eli VanderBilt, Aniruddha Kembhavi, Carl Vondrick, Georgia Gkioxari, Kiana Ehsani, Ludwig Schmidt, and Ali Farhadi. Objaverse-xl: A universe of 10m+ 3d objects. *arXiv preprint arXiv:2307.05663*, 2023. 15
- [10] Yu Deng, Jiaolong Yang, Jianfeng Xiang, and Xin Tong. Gram: Generative radiance manifolds for 3d-aware image generation. In *IEEE/CVF Conference on Computer Vision and Pattern Recognition*, 2022. 2
- [11] Laura Downs, Anthony Francis, Nate Koenig, Brandon Kinman, Ryan Michael Hickman, Krista Reymann, Thomas Barlow McHugh, and Vincent Vanhoucke. Google scanned objects: A high-quality dataset of 3d scanned household items. *2022 International Conference on Robotics and Automation (ICRA)*, pages 2553–2560, 2022. 7, 16
- [12] Jun Gao, Tianchang Shen, Zian Wang, Wenzheng Chen, Kangxue Yin, Daiqing Li, Or Litany, Zan Gojcic, and Sanja Fidler. Get3d: A generative model of high quality 3d textured shapes learned from images. In *Advances In Neural Information Processing Systems*, 2022. 2
- [13] Github user estheryang11. ReconViaGen. <https://github.com/estheryang11/ReconViaGen>, 2025. GitHub repository, accessed 2026-01-22. 15
- [14] Xianglong He, Junyi Chen, Sida Peng, Di Huang, Yangguang Li, Xiaoshui Huang, Chun Yuan, Wanli Ouyang, and Tong He. Gvgen: Text-to-3d generation with volumetric representation. In *Computer Vision – ECCV 2024: 18th European Conference, Milan, Italy, September 29–October 4, 2024, Proceedings, Part VIII*, page 463–479, Berlin, Heidelberg, 2024. Springer-Verlag. 2
- [15] Yicong Hong, Kai Zhang, Jiuxiang Gu, Sai Bi, Yang Zhou, Difan Liu, Feng Liu, Kalyan Sunkavalli, Trung Bui, and Hao Tan. LRM: Large reconstruction model for single image to 3d. In *The Twelfth International Conference on Learning Representations*, 2024. 3
- [16] Jingyu Hu, Ka-Hei Hui, Zhengzhe Liu, Ruihui Li, and Chi-Wing Fu. Neural wavelet-domain diffusion for 3d shape generation, inversion, and manipulation. *ACM Trans. Graph.*, 43(2), 2024. 2
- [17] Binbin Huang, Haobin Duan, Yiqun Zhao, Zibo Zhao, Yi Ma, and Shenghua Gao. Cupid: Pose-grounded generative 3d reconstruction from a single image. *arXiv preprint arXiv:2510.20776*, 2025. 2, 3
- [18] Jiaxin Huang, Yuanbo Yang, Bangbang Yang, Lin Ma, Yuewen Ma, and Yiyi Liao. Gen3r: 3d scene generation meets feed-forward reconstruction. *ArXiv*, abs/2601.04090, 2026. 3
- [19] Hanwen Jiang, Zhenyu Jiang, Kristen Grauman, and Yuke Zhu. Few-view object reconstruction with unknown categories and camera poses. *International Conference on 3D Vision (3DV)*, 2024. 3
- [20] Hanwen Jiang, Zhenyu Jiang, Yue Zhao, and Qixing Huang. LEAP: Liberate sparse-view 3d modeling from camera poses. In *The Twelfth International Conference on Learning Representations*, 2024. 3
- [21] Lihan Jiang, Yucheng Mao, Linning Xu, Tao Lu, Kerui Ren, Yichen Jin, Xudong Xu, Mulin Yu, Jiangmiao Pang, Feng Zhao, et al. Anysplat: Feed-forward 3d gaussian splatting from unconstrained views. *arXiv preprint arXiv:2505.23716*, 2025. 3
- [22] Cijo Jose, Théo Moutakanni, Dahyun Kang, Federico Baldassarre, Timothée Darcet, Hu Xu, Daniel Li, Marc Szafraniec, Michaël Ramamonjisoa, Maxime Oquab, Oriane Siméoni, Huy V. Vo, Patrick Labatut, and Piotr Bojanowski. Dinov2 meets text: A unified framework for image- and pixel-level vision-language alignment, 2024. 4, 6
- [23] Nikhil Keetha, Norman Müller, Johannes Schönberger, Lorenzo Porzi, Yuchen Zhang, Tobias Fischer, Arno

- Knapitsch, Duncan Zauss, Ethan Weber, Nelson Antunes, Jonathon Luiten, Manuel Lopez-Antequera, Samuel Rota Bulò, Christian Richardt, Deva Ramanan, Sebastian Scherer, and Peter Kotschieder. MapAnything: Universal feed-forward metric 3D reconstruction, 2025. arXiv preprint arXiv:2509.13414. 1, 3
- [24] Bernhard Kerbl, Georgios Kopanas, Thomas Leimkühler, and George Drettakis. 3d gaussian splatting for real-time radiance field rendering. *ACM Transactions on Graphics*, 42(4), 2023. 3
- [25] Mukul Khanna\*, Yongsan Mao\*, Hanxiao Jiang, Sanjay Haresh, Brennan Shacklett, Dhruv Batra, Alexander Clegg, Eric Undersander, Angel X. Chang, and Manolis Savva. Habitat Synthetic Scenes Dataset (HSSD-200): An Analysis of 3D Scene Scale and Realism Tradeoffs for ObjectGoal Navigation. *arXiv preprint*, 2023. 15
- [26] Diederik P. Kingma and Jimmy Ba. Adam: A method for stochastic optimization. *CoRR*, abs/1412.6980, 2014. 15
- [27] Vincent Lepetit, Francesc Moreno-Noguer, and Pascal Fua. Eppn: An accurate o(n) solution to the pnp problem. *Int. J. Comput. Vision*, 81(2):155–166, 2009. 2
- [28] Baicheng Li, Dong Wu, Jun Li, Shunkai Zhou, Zecui Zeng, Lusong Li, and Hongbin Zha. Mv-sam3d: Adaptive multi-view fusion for layout-aware 3d generation. *arXiv preprint arXiv:2603.11633*, 2026. 7, 15
- [29] Weiyu Li, Jiarui Liu, Hongyu Yan, Rui Chen, Yixun Liang, Xuelin Chen, Ping Tan, and Xiaoxiao Long. Craftsman3d: High-fidelity mesh generation with 3d native diffusion and interactive geometry refiner. In *Proceedings of the IEEE/CVF Conference on Computer Vision and Pattern Recognition (CVPR)*, pages 5307–5317, 2025. 2, 3
- [30] Zhihao Li, Yufei Wang, Heliang Zheng, Yihao Luo, and Bihan Wen. Sparc3d: Sparse representation and construction for high-resolution 3d shapes modeling. *arXiv preprint arXiv:2505.14521*, 2025. 2, 3
- [31] Weixin Liang, Lili Yu, Liang Luo, Srini Iyer, Ning Dong, Chunting Zhou, Gargi Ghosh, Mike Lewis, Wen tau Yih, Luke Zettlemoyer, and Xi Victoria Lin. Mixture-of-transformers: A sparse and scalable architecture for multi-modal foundation models. *Transactions on Machine Learning Research*, 2025. 2, 4, 5, 8
- [32] Haotong Lin, Sili Chen, Jun Hao Liew, Donny Y. Chen, Zhenyu Li, Guang Shi, Jiashi Feng, and Bingyi Kang. Depth anything 3: recovering the visual space from any views. *arXiv preprint arXiv:2511.10647*, 2025. 1
- [33] Yaron Lipman, Ricky T. Q. Chen, Heli Ben-Hamu, Maximilian Nickel, and Matthew Le. Flow matching for generative modeling. In *The Eleventh International Conference on Learning Representations*, 2023. 3, 4
- [34] Shitong Luo and Wei Hu. Diffusion probabilistic models for 3d point cloud generation. In *2021 IEEE/CVF Conference on Computer Vision and Pattern Recognition (CVPR)*, pages 2836–2844, 2021. 2
- [35] Ben Mildenhall, Pratul P. Srinivasan, Matthew Tancik, Jonathan T. Barron, Ravi Ramamoorthi, and Ren Ng. Nerf: Representing scenes as neural radiance fields for view synthesis. In *ECCV*, 2020. 3
- [36] Norman Müller, Yawar Siddiqui, Lorenzo Porzi, Samuel Rota Bulò, Peter Kotschieder, and Matthias Nießner. Diffrf: Rendering-guided 3d radiance field diffusion. In *Proceedings of the IEEE/CVF Conference on Computer Vision and Pattern Recognition*, pages 4328–4338, 2023. 2
- [37] Maxime Oquab, Timothée Darcet, Theo Moutakanni, Huy V. Vo, Marc Szafraniec, Vasil Khalidov, Pierre Fernandez, Daniel Haziza, Francisco Massa, Alaaeldin El-Nouby, Russell Howes, Po-Yao Huang, Hu Xu, Vasu Sharma, Shang-Wen Li, Wojciech Galuba, Mike Rabbat, Mido Assran, Nicolas Ballas, Gabriel Synnaeve, Ishan Misra, Herve Jegou, Julien Mairal, Patrick Labatut, Armand Joulin, and Piotr Bojanowski. Dinov2: Learning robust visual features without supervision, 2023. 4, 6
- [38] Stanislav Pidhorskyi, Tomas Simon, Gabriel Schwartz, He Wen, Yaser Sheikh, and Jason Saragih. Rasterized edge gradients: Handling discontinuities differentially. *arXiv preprint arXiv:2405.02508*, 2024. 6, 14
- [39] Charles R Qi, Li Yi, Hao Su, and Leonidas J Guibas. Pointnet++: Deep hierarchical feature learning on point sets in a metric space. *arXiv preprint arXiv:1706.02413*, 2017. 15
- [40] Robin Rombach, Andreas Blattmann, Dominik Lorenz, Patrick Esser, and Björn Ommer. High-resolution image synthesis with latent diffusion models. In *Proceedings of the IEEE/CVF Conference on Computer Vision and Pattern Recognition (CVPR)*, pages 10684–10695, 2022. 2, 3
- [41] Shunsuke Saito, Zeng Huang, Ryota Natsume, Shigeo Morishima, Angjoo Kanazawa, and Hao Li. Pifu: Pixel-aligned implicit function for high-resolution clothed human digitization. In *Proceedings of the IEEE/CVF International Conference on Computer Vision (ICCV)*, 2019. 3
- [42] Shunsuke Saito, Tomas Simon, Jason Saragih, and Hanbyul Joo. Pifuhd: Multi-level pixel-aligned implicit function for high-resolution 3d human digitization. In *CVPR*, 2020. 3
- [43] SAM3DTeam, Xingyu Chen, Fu-Jen Chu, Pierre Gleize, Kevin J Liang, Alexander Sax, Hao Tang, Weiyao Wang, Michelle Guo, Thibaut Hardin, Xiang Li, Aohan Lin, Jiawei Liu, Ziqi Ma, Anushka Sagar, Bowen Song, Xiaodong Wang, Jianing Yang, Bowen Zhang, Piotr Dollár, Georgia Gkioxari, Matt Feiszli, and Jitendra Malik. Sam 3d: 3dfy anything in images. 2025. 3, 15
- [44] Johannes Lutz Schönberger and Jan-Michael Frahm. Structure-from-motion revisited. In *Conference on Computer Vision and Pattern Recognition (CVPR)*, 2016. 1
- [45] Johannes Lutz Schönberger, Enliang Zheng, Marc Pollefeys, and Jan-Michael Frahm. Pixelwise view selection for unstructured multi-view stereo. In *European Conference on Computer Vision (ECCV)*, 2016. 1
- [46] Philipp Schröppel, Christopher Wewer, Jan Eric Lenssen, Eddy Ilg, and Thomas Brox. Neural point cloud diffusion for disentangled 3d shape and appearance generation. In *CVPR*, 2024. 2
- [47] J. Ryan Shue, Eric Ryan Chan, Ryan Po, Zachary Ankner, Jiajun Wu, and Gordon Wetzstein. 3d neural field generation using triplane diffusion. In *Proceedings of the IEEE/CVF Conference on Computer Vision and Pattern Recognition (CVPR)*, pages 20875–20886, 2023. 2

- [48] Ivan Skorokhodov, Aliaksandr Siarohin, Yinghao Xu, Jian Ren, Hsin-Ying Lee, Peter Wonka, and Sergey Tulyakov. 3d generation on imagenet. In *International Conference on Learning Representations*, 2023. 2
- [49] Stefan Stojanov, Anh Thai, and James M. Rehg. Using shape to categorize: Low-shot learning with an explicit shape bias. 2021. 7, 16
- [50] Zhicong Tang, Shuyang Gu, Chunyu Wang, Ting Zhang, Jianmin Bao, Dong Chen, and Baining Guo. Volumediffusion: Flexible text-to-3d generation with efficient volumetric encoder, 2023. 2
- [51] Tencent Hunyuan3D Team. Hunyuan3d 1.0: A unified framework for text-to-3d and image-to-3d generation, 2024. 2, 3
- [52] Tencent Hunyuan3D Team. Hunyuan3d 2.0: Scaling diffusion models for high resolution textured 3d assets generation, 2025. 18
- [53] Tencent Hunyuan3D Team. Hunyuan3d 2.5: Towards high-fidelity 3d assets generation with ultimate details, 2025. 2, 3, 18
- [54] Jianyuan Wang, Christian Rupprecht, and David Novotny. PoseDiffusion: Solving pose estimation via diffusion-aided bundle adjustment. 2023. 8
- [55] Jianyuan Wang, Minghao Chen, Nikita Karaev, Andrea Vedaldi, Christian Rupprecht, and David Novotny. Vggt: Visual geometry grounded transformer. In *Proceedings of the IEEE/CVF Conference on Computer Vision and Pattern Recognition*, 2025. 1, 2, 3, 4, 5, 14
- [56] Peng Wang, Hao Tan, Sai Bi, Yinghao Xu, Fujun Luan, Kalyan Sunkavalli, Wenping Wang, Zexiang Xu, and Kai Zhang. PF-LRM: Pose-free large reconstruction model for joint pose and shape prediction. In *The Twelfth International Conference on Learning Representations*, 2024. 3
- [57] Qianqian Wang, Yifei Zhang, Aleksander Holynski, Alexei A. Efros, and Angjoo Kanazawa. Continuous 3d perception model with persistent state. In *Proceedings of the IEEE/CVF Conference on Computer Vision and Pattern Recognition (CVPR)*, pages 10510–10522, 2025. 3
- [58] Shuzhe Wang, Vincent Leroy, Yohann Cabon, Boris Chidlovskii, and Jerome Revaud. Dust3r: Geometric 3d vision made easy. In *Proceedings of the IEEE/CVF Conference on Computer Vision and Pattern Recognition (CVPR)*, pages 20697–20709, 2024. 3
- [59] Tengfei Wang, Bo Zhang, Ting Zhang, Shuyang Gu, Jianmin Bao, Tadas Baltrusaitis, Jingjing Shen, Dong Chen, Fang Wen, Qifeng Chen, and Baining Guo. Rodin: A generative model for sculpting 3d digital avatars using diffusion. In *Proceedings of the IEEE/CVF Conference on Computer Vision and Pattern Recognition (CVPR)*, pages 4563–4573, 2023. 2
- [60] Weijie Wang, Yeqing Chen, Zeyu Zhang, Hengyu Liu, Haoxiao Wang, Zhiyuan Feng, Wenkang Qin, Zheng Zhu, Donny Y. Chen, and Bohan Zhuang. Volsplat: Rethinking feed-forward 3d gaussian splatting with voxel-aligned prediction. *arXiv preprint arXiv:2509.19297*, 2025. 3
- [61] Yifan Wang, Jianjun Zhou, Haoyi Zhu, Wenzheng Chang, Yang Zhou, Zizun Li, Junyi Chen, Jiangmiao Pang, Chunhua Shen, and Tong He.  $\pi^3$ : Scalable permutation-equivariant visual geometry learning, 2025. 1, 2, 3, 5, 14
- [62] Guanjun Wu, Jiemin Fang, Chen Yang, Sikuang Li, Taoran Yi, Jia Lu, Zanwei Zhou, Jiazhong Cen, Lingxi Xie, Xiaopeng Zhang, Wei Wei, Wenyu Liu, Xinggong Wang, and Qi Tian. Unilat3d: Geometry-appearance unified latents for single-stage 3d generation. *arXiv preprint arXiv:2509.25079*, 2025. 2, 3, 8, 15
- [63] Jiajun Wu, Chengkai Zhang, Tianfan Xue, William T. Freeman, and Joshua B. Tenenbaum. Learning a probabilistic latent space of object shapes via 3d generative-adversarial modeling. In *Proceedings of the 30th International Conference on Neural Information Processing Systems*, page 82–90, Red Hook, NY, USA, 2016. Curran Associates Inc. 2
- [64] Shuang Wu, Youtian Lin, Feihu Zhang, Yifei Zeng, Jingxi Xu, Philip Torr, Xun Cao, and Yao Yao. Direct3d: scalable image-to-3d generation via 3d latent diffusion transformer. In *Proceedings of the 38th International Conference on Neural Information Processing Systems*, Red Hook, NY, USA, 2024. Curran Associates Inc. 2, 3
- [65] Shuang Wu, Youtian Lin, Feihu Zhang, Yifei Zeng, Yikang Yang, Yajie Bao, Jiachen Qian, Siyu Zhu, Philip Torr, Xun Cao, and Yao Yao. Direct3d-s2: Gigascale 3d generation made easy with spatial sparse attention. *arXiv preprint arXiv:2505.17412*, 2025. 2, 3
- [66] Tong Wu, Jiarui Zhang, Xiao Fu, Yuxin Wang, Liang Pan, Jiawei Ren, Wayne Wu, Lei Yang, Jiaqi Wang, Chen Qian, Dahua Lin, and Ziwei Liu. Omniobject3d: Large-vocabulary 3d object dataset for realistic perception, reconstruction and generation. In *IEEE/CVF Conference on Computer Vision and Pattern Recognition (CVPR)*, 2023. 17
- [67] Jianfeng Xiang, Xiaoxue Chen, Sicheng Xu, Ruicheng Wang, Zelong Lv, Yu Deng, Hongyuan Zhu, Yue Dong, Hao Zhao, Nicholas Jing Yuan, and Jiaolong Yang. Native and compact structured latents for 3d generation. *Tech report*, 2025. 2, 18
- [68] Jianfeng Xiang, Zelong Lv, Sicheng Xu, Yu Deng, Ruicheng Wang, Bowen Zhang, Dong Chen, Xin Tong, and Jiaolong Yang. Structured 3d latents for scalable and versatile 3d generation. In *Proceedings of the IEEE/CVF Conference on Computer Vision and Pattern Recognition (CVPR)*, pages 21469–21480, 2025. 2, 3, 5, 6, 8, 15
- [69] Yuliang Xiu, Jinlong Yang, Dimitrios Tzionas, and Michael J. Black. ICON: Implicit Clothed humans Obtained from Normals. In *Proceedings of the IEEE/CVF Conference on Computer Vision and Pattern Recognition (CVPR)*, pages 13296–13306, 2022. 3
- [70] Yuliang Xiu, Jinlong Yang, Xu Cao, Dimitrios Tzionas, and Michael J. Black. ECON: Explicit Clothed humans Optimized via Normal integration. In *Proceedings of the IEEE/CVF Conference on Computer Vision and Pattern Recognition (CVPR)*, 2023. 3
- [71] Chao Xu, Ang Li, Linghao Chen, Yulin Liu, Ruoxi Shi, Hao Su, and Minghua Liu. Sparp: Fast 3d object reconstruction and pose estimation from sparse views. In *Computer Vision – ECCV 2024*, pages 143–163, Cham, 2024. Springer Nature Switzerland. 3
- [72] Jiale Xu, Weihao Cheng, Yiming Gao, Xintao Wang, Shenghua Gao, and Ying Shan. InstantMesh: Efficient 3d

mesh generation from a single image with sparse-view large reconstruction models. *arXiv preprint arXiv:2404.07191*, 2024. 3

- [73] Jiale Xu, Shenghua Gao, and Ying Shan. Freesplatter: Pose-free gaussian splatting for sparse-view 3d reconstruction. *arXiv preprint arXiv:2412.09573*, 2024. 3
- [74] Kaixin Yao, Longwen Zhang, Xinhao Yan, Yan Zeng, Qixuan Zhang, Lan Xu, Wei Yang, Jiayuan Gu, and Jingyi Yu. Cast: Component-aligned 3d scene reconstruction from an rgb image. *ACM Trans. Graph.*, 44(4), 2025. 3
- [75] Chongjie Ye, Yushuang Wu, Ziteng Lu, Jiahao Chang, Xiaoyang Guo, Jiaqing Zhou, Hao Zhao, and Xiaoguang Han. Hi3dgen: High-fidelity 3d geometry generation from images via normal bridging. *arXiv preprint arXiv:2503.22236*, 2025. 2, 3
- [76] Biao Zhang, Jiapeng Tang, Matthias Nießner, and Peter Wonka. 3dshape2vecset: A 3d shape representation for neural fields and generative diffusion models. *ACM Trans. Graph.*, 42(4), 2023. 3
- [77] Bowen Zhang, Yiji Cheng, Chunyu Wang, Ting Zhang, Jiaolong Yang, Yansong Tang, Feng Zhao, Dong Chen, and Baining Guo. Rodinhd: High-fidelity 3d avatar generation with diffusion models. In *Computer Vision – ECCV 2024: 18th European Conference, Milan, Italy, September 29–October 4, 2024, Proceedings, Part XIV*, page 465–483, Berlin, Heidelberg, 2024. Springer-Verlag. 2
- [78] Bowen Zhang, Yiji Cheng, Jiaolong Yang, Chunyu Wang, Feng Zhao, Yansong Tang, Dong Chen, and Baining Guo. Gaussiancube: Structuring gaussian splatting using optimal transport for 3d generative modeling. 2024. 2
- [79] Junyi Zhang, Charles Herrmann, Junhwa Hur, Varun Jampani, Trevor Darrell, Forrester Cole, Deqing Sun, and Ming-Hsuan Yang. MonST3r: A simple approach for estimating geometry in the presence of motion. In *The Thirteenth International Conference on Learning Representations*, 2025. 3
- [80] Longwen Zhang, Ziyu Wang, Qixuan Zhang, Qiwei Qiu, Anqi Pang, Haoran Jiang, Wei Yang, Lan Xu, and Jingyi Yu. Clay: A controllable large-scale generative model for creating high-quality 3d assets. *ACM Transactions on Graphics (TOG)*, 43(4):1–20, 2024. 3
- [81] Richard Zhang, Phillip Isola, Alexei A Efros, Eli Shechtman, and Oliver Wang. The unreasonable effectiveness of deep features as a perceptual metric. In *CVPR*, 2018. 8
- [82] Xin-Yang Zheng, Yang Liu, Peng-Shuai Wang, and Xin Tong. Sdf-stylegan: Implicit sdf-based stylegan for 3d shape generation. In *Comput. Graph. Forum (SGP)*, 2022. 2
- [83] Haoyi Zhu, Yifan Wang, Jianjun Zhou, Wenzheng Chang, Yang Zhou, Zizun Li, Junyi Chen, Chunhua Shen, Jiangmiao Pang, and Tong He. Aether: Geometric-aware unified world modeling. In *Proceedings of the IEEE/CVF International Conference on Computer Vision (ICCV)*, pages 8535–8546, 2025. 3

## S1. Implementation and Evaluation Details

### S1.1. Block Matching Algorithm

In Sec. 3.3, we designed a block matching strategy which ultimately led to the exact matching Fig. 2. Here, we explain the exact algorithm to derive the specific matching.

According to our matching principle that each global  $\pi^3$  block must be matched with a TRELIS block, we compute a uniform index injection from all the 18 global blocks of  $\pi^3$  into the 24 blocks of TRELIS. Let  $P_l (l = 0, \dots, 35)$  and  $T_j (j = 0, \dots, 24)$  denote the blocks of  $\pi^3$  and TRELIS, respectively. Then a simple computation according to the rule above yields the following one-to-one matching:  $T_0, T_1, T_2, T_4, T_5, T_6, T_8, T_9, T_{10}, T_{12}, T_{13}, T_{14}, T_{16}, T_{17}, T_{18}, T_{20}, T_{21}, T_{23}$  and  $P_1, P_3, P_5, P_7, P_9, P_{11}, P_{13}, P_{15}, P_{17}, P_{19}, P_{21}, P_{23}, P_{25}, P_{27}, P_{29}, P_{31}, P_{33}, P_{35}$ . Now there remain 6 unmatched TRELIS blocks. The matched pairs become type-C mixtures. Note that there is only a unique way to insert them into the original sequence in an order-preserving way. For example, to insert  $T_3$  between matched pairs  $(T_2, P_5)$  and  $(T_4, P_7)$ , we must match  $T_3$  and  $P_6$ . The same goes for all unmatched TRELIS blocks, giving us type-B mixtures between  $T_3, T_7, T_{11}, T_{15}, T_{19}, T_{22}$  and  $P_6, P_{12}, P_{18}, P_{24}, P_{30}, P_{34}$ . Finally, the remaining unmatched  $\pi^3$  blocks become type-A blocks. Note that there might be other plausible matchings, but exhausting them is neither practical nor our main focus.

### S1.2. Camera Intrinsic Estimation

In the alignment evaluation, all generated models are rendered back to the input view for evaluation, which requires estimating camera intrinsics. ReconViaGen [3] uses VGGT [55] which already estimates intrinsics. Our model is based on  $\pi^3$  [61] which predicts only extrinsics and local point map. To estimate the intrinsic matrix  $K$ , we solve for  $f_x, f_y, c_x, c_y$  from the following equation:

$$u = f_x x / z + c_x; \quad (11)$$

$$v = f_y y / z + c_y, \quad (12)$$

which is equivalent to

$$\begin{bmatrix} x/z & 0 & 1 & 0 \\ 0 & y/z & 0 & 1 \end{bmatrix} \begin{bmatrix} f_x \\ f_y \\ c_x \\ c_y \end{bmatrix} = \begin{bmatrix} u \\ v \end{bmatrix}. \quad (13)$$

Here,  $(u, v)$  and  $(x, y, z)$  ranges over all foreground pixels and 3D points in the output point map of  $\pi^3$ , leading to an overdetermined equation which we solve in the least-squares sense. This intrinsic is used as an initial value and then refined by differentiable rendering using DRTK [38]. During the differentiable rendering refinement, we parameterize the camera focal as  $f = \exp(l)$  and use quaternions to

represent camera rotation. The optimization uses the Adam optimizer [26] and runs for 2000 steps with a learning rate of  $10^{-2}$ . We apply early stopping if the loss has not decreased for 100 steps.

Note that SAM3D [43] only predicts the object in the camera space without intrinsics. Unlike  $\pi^3$ , SAM3D does not have a pixel-wise 2D-3D correspondence. Hence, we match the extreme values of  $x/z$  and  $y/z$  to the input image foreground bounding box to estimate the intrinsics and extrinsics for SAM3D.

### S1.3. Dataset

To train our model, we use the TRELIS-500k dataset [68], which is composed of selected models from Objaverse-XL [9], ABO [7] and HSSD [25]. Our joint 3D generation and camera estimation pipeline requires ground truth sparse structure latents and structured latents, together with their paired multi-view renderings and camera parameters. However, following the full dataset processing pipeline in TRELIS requires significant computational resources. Thus, we use only 8-view renderings of each item to directly generate these paired data samples using TRELIS [68]. Finally, after excluding a part of models that either take too long to render or cause generation failures, we generated 404354 objects, each paired with their GT latent codes and 32 renderings densely covering the upper hemisphere with varying focal lengths.

### S1.4. Model and Training

At each training step, we randomly sample an object and 4 views from its 32 renderings. To better cover different view configurations, we use a mixture of the following 3 view sampling modes. (1) Fully random sampling: we randomly choose 4 views without replacement with a uniform distribution. (2) Nearest-view sampling: we first randomly select one view, and then sample its nearest 3 views (“nearest” in terms of camera positions). (3) Farthest-view sampling: we start with a random view and use farthest point sampling [39] (in terms of camera positions). The probabilities of choosing these three modes are 0.2, 0.4, 0.4, respectively. For training, we use pretrained weights of the TRELIS sparse structure flow model for our 3D branch, and the pretrained weights of  $\pi^3$  for the 2D branch. For the MoT self-attention modules, we load pretrained weights from either TRELIS or  $\pi^3$  whenever possible. During training, we only activate the following parameters: (1) all parameters without a pretrained weight; (2) all parameters of cross-attention modules and MoT self-attention modules. Our core model involved in training (excluding the DINOv2 encoder and the sparse structure VAE decoder) contains 1.71B parameters in total and 839.78M trainable parameters.

We use a learning rate of  $10^{-4}$  with cosine scheduling and train for 400k steps with a batch size of 16. The training

runs on 16 NVIDIA-A100 GPUs and takes about one week.

## S1.5. Evaluation Settings for Baselines

For ReconViaGen [3], we use an open-source implementation [13]. For SAM3D [43], we use an open-source training-free extension to the multi-view setting [28], which adopts weighted multi-diffusion to better fuse multi-view information. To adapt TRELIS and UniLat3D to multi-view inputs, we follow the official repositories to use the `run_multi_image` API, which adopts stochastic image condition sampling to inject multi-view information. Note that the comparison is fair in the sense that (1) both TRELIS and UniLat3D use the same input views as ours; (2) Our stage-2 model also uses stochastic sampling. The only difference in conditioning is that our stage-1 model uses all-view tokens, which we had attempted for the baselines for fairness, but we found this led to worse baseline performance, so we kept their stochastic sampling.

In our evaluation of geometry and texture accuracy, we need to align all generated shapes to GT ones. However, since generated shapes may not have the exact orientation and scale as the GT ones, we use a heuristic method to achieve this alignment as follows.

For methods that come with camera pose estimations (ours, ReconViaGen and SAM3D), we first compute a rotation between predicted poses and GT poses. This rotation is then applied to the generated object to initialize a good orientation. Then we run ICP from this initialization to get a similarity transformation that provides a more accurate alignment.

For methods that do not estimate pose (TRELIS [68], UniLat3D [62]), we remark that both of them has  $+z$  as the “up” direction, and their “front” direction is aligned to either the  $x$ -axis or the  $y$ -axis. Observing this, we first try out 4 different orientations in the  $xy$ -plane and find the one with minimal Chamfer distance. Then ICP is run from this initialization to get the final alignment geometry.

## S2. Extended Evaluations

### S2.1. Evaluation of Model Components

In this section we show the effectiveness of several of our technical choices. Note that our stage-1 model is a minimal architecture in the sense that we cannot ablate a part without breaking the whole pipeline. For example, if we remove either the TRELIS branch, the  $\pi^3$  branch or the alignment transformation branch, we wouldn’t have aligned voxels and points for stage-2 generation. Also, if we remove the MoT self-attentions, there wouldn’t be information exchange to make the aligned training well-defined. Thus, instead of directly ablating the individual branches in our mixed model, we use the following experiments to demonstrate the effectiveness of our mixture design as a whole.

Table S4. Separate evaluation of our stage-1 model and our stage-2 model.

|         |         | Toys4k        |               |              |                         |
|---------|---------|---------------|---------------|--------------|-------------------------|
| Stage-1 | Stage-2 | PSNR          | SSIM          | LPIPS        | CD ( $\times 10^{-3}$ ) |
| TRELLIS | TRELLIS | 23.930        | 0.9311        | 0.055        | 7.9986                  |
| Ours    | TRELLIS | 26.975        | 0.9527        | 0.035        | <b>0.7259</b>           |
| Ours    | Ours    | <b>27.177</b> | <b>0.9551</b> | <b>0.033</b> | 0.7419                  |
|         |         | GSO           |               |              |                         |
| Stage-1 | Stage-2 | PSNR          | SSIM          | LPIPS        | CD ( $\times 10^{-3}$ ) |
| TRELLIS | TRELLIS | 22.420        | 0.9034        | 0.079        | 4.5658                  |
| Ours    | TRELLIS | 24.399        | 0.9199        | 0.062        | 0.8010                  |
| Ours    | Ours    | <b>24.826</b> | <b>0.9271</b> | <b>0.055</b> | <b>0.7945</b>           |

Table S5. Evaluation of point map errors ( $\times 10^{-3}$ ).

|         |              | Toys4k       |              | GSO          |  |
|---------|--------------|--------------|--------------|--------------|--|
| Method  | PE           | CD           | PE           | CD           |  |
| $\pi^3$ | 9.441        | 3.753        | 6.723        | 2.896        |  |
| Ours    | <b>2.285</b> | <b>0.527</b> | <b>3.729</b> | <b>1.258</b> |  |

To evaluate the effectiveness of our aligned voxel generation and point map prediction, we compare our stage-1 model and that of TRELLIS, using the "Geometry and texture accuracy" evaluation protocol in Sec. 4.2 to first align generations to GT before computing metrics. The results are reported in Table S4. Our stage-1 model produces input-consistent voxels, leading to notable metric improvements even with the TRELLIS stage-2 model. Furthermore, since the stage-1 generation already determines the coarse geometry, our stage-2 generation is more effective for texture alignment. Note that the combination of TRELLIS stage-1 plus our stage-2 is not feasible since TRELLIS does not produce voxel-aligned point maps, so this combination is not evaluated.

To show that our MoT-based architecture also conversely benefits the point map prediction, we evaluate the point map accuracy of our model and that of  $\pi^3$ , using pixel-wise error (PE) and Chamfer distance (CD), both computed after a similarity transformation alignment. The results are shown in Table S5.

Finally, we evaluate the usage of attention biases and camera refinement. Table S6 shows the metrics of our method after removing camera refinement and attention bias. Even though the metric improvement brought by using our attention bias seems minor, the improvement can be more clearly observed with qualitative examples. Fig. S9 shows cases where our attention bias notably improves texture alignment. Note that this type of improvement often happens to rotationally symmetric objects with asymmetric texture. However, in both Toys4k [49] and GSO [11] there are only limited cases like this. This is why our attention

Table S6. Ablations of attention bias and camera refinement.

| Attn Bias | Refine | PSNR   | SSIM   | LPIPS |
|-----------|--------|--------|--------|-------|
| Dataset   |        | Toys4k |        |       |
| No        | No     | 25.014 | 0.9397 | 0.042 |
| Yes       | No     | 25.163 | 0.9422 | 0.039 |
| Yes       | Yes    | 28.144 | 0.9621 | 0.030 |
| Dataset   |        | GSO    |        |       |
| No        | No     | 23.020 | 0.9039 | 0.078 |
| Yes       | No     | 23.350 | 0.9107 | 0.070 |
| Yes       | Yes    | 25.031 | 0.9281 | 0.057 |

Table S7. Ablations of attention bias and camera refinement on symmetric and asymmetric objects in the GSO dataset.

|           |        | AG (645 objects)   |               |              |
|-----------|--------|--------------------|---------------|--------------|
| Attn Bias | Refine | PSNR               | SSIM          | LPIPS        |
| No        | No     | 24.341             | 0.9293        | 0.052        |
| Yes       | No     | 24.515             | 0.9336        | 0.049        |
| Yes       | Yes    | <b>25.675</b>      | <b>0.9434</b> | <b>0.044</b> |
|           |        | SGAT (279 objects) |               |              |
| Attn Bias | Refine | PSNR               | SSIM          | LPIPS        |
| No        | No     | 20.849             | 0.8578        | 0.112        |
| Yes       | No     | 21.654             | 0.8724        | 0.093        |
| Yes       | Yes    | <b>23.207</b>      | <b>0.8958</b> | <b>0.077</b> |
|           |        | SGST (97 objects)  |               |              |
| Attn Bias | Refine | PSNR               | SSIM          | LPIPS        |
| No        | No     | 20.303             | 0.8644        | 0.150        |
| Yes       | No     | 20.328             | 0.8661        | 0.149        |
| Yes       | Yes    | <b>25.923</b>      | <b>0.9178</b> | <b>0.094</b> |

bias has a marginal metric improvement but remains important and effective in improving texture alignment in multi-view settings. To further verify this, we manually annotated items in the GSO dataset as "Asymmetric-Geometry (AG)", "Symmetric-Geometry Asymmetric-Texture (SGAT)" and "Symmetric-Geometry Symmetric-Texture (SGST)". Note that we only consider rotational symmetry (balls, square boxes, bottles, etc.), since mirror symmetry can be visually disambiguated from only the geometry. Table S7 shows the metric results. Our proposed attention bias in stage-2 is indeed most effective on SGAT objects.

The ablations on attention bias and camera refinement are shown in Fig. S6.

## S2.2. Runtime Report

For all our experiments, we use an input image resolution of 518, and we run 50 steps for stage-1 generation, and 25 steps for stage-2 generation. With 4 input views, on a single NVIDIA-A100 GPU, our stage-1 generation takes around 30s, and our stage-2 generation generally takes around 3~10s, depending on the number of voxels gener-

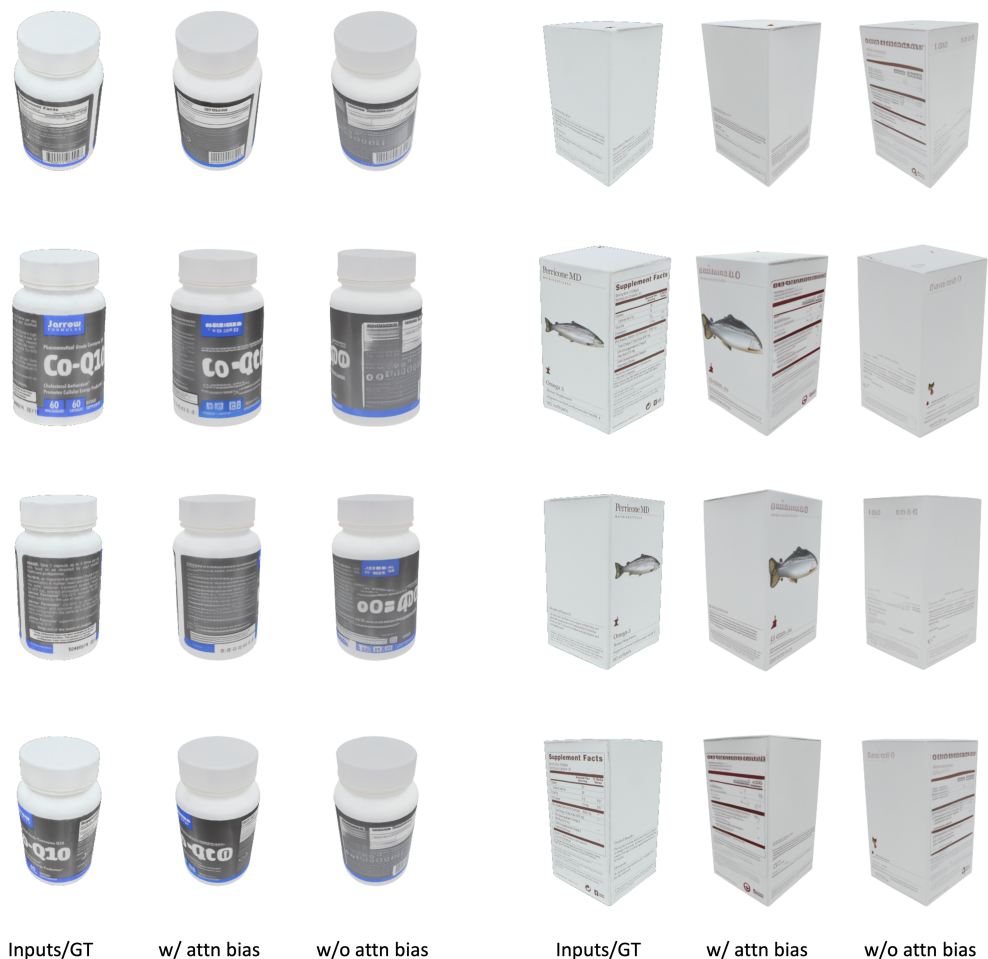


Figure S9. Qualitative studies of ablating our proposed attention bias.

ated in stage 1. The attention bias computation generally takes  $<10s$ . The camera refinement process takes no more than  $10s$  per view. Note that this is not needed if accurate poses are not required.

### S3. Extended Discussions on Limitations

In this section, we provide further discussions on the limitations of our method and possible future directions.

**Degradation caused by view configuration** While our method utilizes  $\pi^3$  to provide geometrically informative features, different view configurations can impact how well the  $\pi^3$  branch aligns different view points. Generally, the best performance can be obtained if all views are directly looking at the center of the object with a zero roll angle. However, in real-world scenarios it is difficult to strictly follow this rule, and therefore performance degradation may

happen if the input view configuration deviates too much from its training distribution. Future work should attempt training with a more diverse view distribution or utilize data augmentation to improve the robustness.

**Limitations of using generated data** As mentioned in Sec. 4.1, our model is trained on TRELIS-generated data due to the extreme high cost of running the original data processing pipeline of TRELIS. These generated models do not contain lighting or view-dependent visual effects. As a result, our method has degraded performance for datasets with highly non-uniform lighting, e.g., OmniObject3D [66], or specular objects. An example is shown in Fig. S10, where dark shadows appear on the side views of the object. Our  $\pi^3$  branch, not trained on these lighting conditions, cannot correctly match the image features through its attention mechanism. As a result, the final generation can neither

benefit much from features of the  $\pi^3$  branch, nor from the attention bias tuning which requires accurate overlap. We believe training with high quality data containing diverse lighting can remedy this issue.

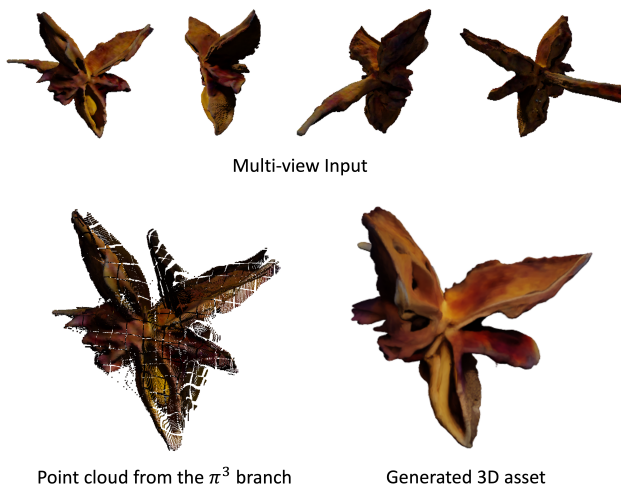


Figure S10. A failure case caused by non-uniform lighting.

**Frozen TRELIS decoders** Our model keeps all the TRELIS VAE decoders frozen. In other words, the latent spaces of TRELIS impose an upper bound for our generation quality. For certain types of textures, e.g., texts or logos on commercial products, even reconstructing them using the TRELIS VAE is problematic. This also limits the faithfulness of geometry or texture preservation of our model. However, since MoT architectures can be easily inserted into different transformers, a possible future direction is to extend our designs to more powerful backbones [52, 53, 67].